Title: Nanoconfined-liquid-dependent water-responsive actuation of *Bacillus subtilis* cell walls

Authors: Seungri Kim[1,2], Haozhen Wang[2,3], Darjan Podbevšek[2], Tong Wang[2], Xi Chen[1,2,3,4*]

Affiliations:

[1]Department of Chemical Engineering, The City College of New York, New York, New York, USA.

[2]Advanced Science Research Center (ASRC), The City University of New York, New York, USA.

[3]PhD Program in Physics, The Graduate Center of the City University of New York, New York, New York, USA.

[4]PhD Program in Chemistry, The Graduate Center of the City University of New York, New York, New York, USA.

*Correspondence to: xchen@gc.cuny.edu

Summary:

Water-responsive (WR) materials can exert significant energy when they deform in response to changes in relative humidity (RH). Recent studies on biological WR materials have brought attention to the potential influence of nanoconfined water on their high-energy WR actuation. Here, we investigated the effects of nanoconfined liquids' properties on the WR actuation of *Bacillus (B.) subtilis* cell walls by introducing chaotropic or kosmotropic solutes, known for their impact on the H-bonding network and biomolecule stabilities in aqueous solutions. We discovered that cell walls treated with low-concentration kosmotropic solutes exhibited a significant increase in WR actuation energy density, reaching 103.3 MJ m^{-3}, surpassing that of existing actuators. However, higher concentrations of kosmotropic or chaotropic solutes led to decreased WR performance. Our observations suggest the presence of an optimal range for kosmotropic and chaotropic treatments to enhance WR energy density. These findings could be explained by the impact of the solutes on hydration forces and intermolecular interactions, which affect the ultimate WR pressure. This, in turn, provides a pathway towards achieving superior WR actuation performance and advancing the development of high-work-density actuator materials.

Introduction

Nature has developed materials and structures that undergo water-responsive (WR) actuation, involving expansion and contraction in response to changes in relative humidity (RH). These WR materials play a crucial role in numerous essential biological functionalities, such as seed dispersal[1], reproductive behavior[2], and photoinhibition[3]. For instance, pine cones use WR structures to release their seeds under dry environment[4], and wheat awns open and close to propel the seed into the soil driven by daily RH changes[5]. Recent studies have demonstrated that such kinds of WR actuation could be extremely fast and powerful[6,7]. *Bacillus (B.) subtilis'* cell walls, which are mainly composed of peptidoglycan, display record-high WR actuation energy and power densities of 72 MJ m^{-3} and 9.1 MW m^{-3}, surpassing those of conventional actuator materials and all known muscles[8]. In addition, the WR actuation of the *B. subtilis* cell walls is extremely fast, taking only ~0.1 s for expansion and ~0.2 s for contraction[8]. These natural WR materials hold great potential to be used as high-performance actuators for a broad range of engineering applications, including seed carriers[9], smart windows[10], clothing[11,12], and energy harvesting devices[13]. However, the fundamental physical principles of water-responsiveness and the design criteria that systematically lead to high-performance WR actuation are still poorly understood.

Despite the unclear WR mechanism, our prior studies have provided compelling evidence of the critical role of anomalously high viscosity of nanoconfined water (~16.4 Pa·s) played in the high energy WR actuation of *B. subtilis'* cell walls[8]. This observation aligns with the enhanced H-bonding network observed in high-energy WR peptide crystals[14–16]. Moreover, recent research has shown that hydration forces, resulting from the interactions between nanoconfined water and solid surfaces, play a determinant role in the WR deformation and mechanical properties of the

'hydration solids', such as the *B. subtilis* spores[17,18]. These findings highlight the importance of enhanced water-water and water-material interactions in materials' WR actuation, and thus, adjusting the properties of liquids confined in aqueous pores should substantially affect the WR behavior and performance[19,20].

Salts ranked in the Hofmeister series[21–23] and osmolytes[24–26] have the ability to alter confined water properties and intermolecular interactions. They can be categorized by their effects on macromolecular structures: chaotropes, which tend to disrupt the structure, or kosmotropes, which promote structure formation and stability[27,28]. Despite the ongoing debate regarding the terminology and mechanism through which these chemical substances influence water properties and intermolecular interactions[29,30], their impact on confined liquids and water-material interactions have been extensively studied across diverse material systems[31,32], such as starch[33], protein hydrogels[34], and silk fibroins[35], as well as in synthetic polymers like poly(*N*-isopropylacrylamide)[36] and polyamide[37]. Therefore, we hypothesized that chaotropes and kosmotropes should significantly influence materials' WR behaviors, allowing for a systematic investigation into their mechanisms.

In this study, we explored the effects of nanoconfined liquids on WR actuation of the *B. subtilis* cell wall by employing chaotropic solutes: urea[38] and potassium iodide (KI)[39], and kosmotropic solutes: sucrose[40], potassium sulfate (K_2SO_4)[41], and potassium chloride (KCl)[29] (**Fig. 1a** and **Fig. S1**). Upon treatment with low-concentration solutions, cell walls display distinct WR properties. For instance, cell walls treated with kosmotropic solutes such as sucrose and K_2SO_4 initially show an increase in WR energy density as the solute concentration rises to 10 mM. However, their

energy densities subsequently decrease as the concentration further increases to 50 mM. In contrast, cell walls treated with chaotropic urea and KI solutions show a monotonic decrease in WR energy density as the concentration increases from 10 mM to 50 mM. The observed trends in WR energy density strongly correlate with the WR pressure of these treated cell walls. We also found that the water-responsiveness of cell walls, including those treated with low-concentration solutes, aligns with the newly discovered theory of hydration solids[17], both in terms of relative size change with RH and the molecular length scale estimated from the data. Our findings suggest that even minor alterations in the properties of nanoconfined liquids can lead to significant changes in WR actuation. These findings not only shed light on the general WR mechanism but also suggest opportunities for optimizing the energy conversion of WR actuation through controlled manipulation of nanoconfined liquids.

Results

Macroscale water-responsiveness of untreated and solute-treated cell-wall-adhesive/Mylar bilayers

The influence of chaotropic and kosmotropic solutes on the water-responsiveness of cell walls was first studied by monitoring macroscopic curvature changes in cell-wall-adhesive/Mylar bilayers. To create these bilayers, we mixed the cell walls with a commercial glue and coated a 9-μm-thick (dry thickness) layer of cell-wall-adhesive composite onto 25-μm-thick Mylar films, using established methods (**Fig. 1b**)[8]. The resulting bilayer films were then immersed in solutions of various concentrations (1 mM, 10 mM, 30 mM, and 50 mM) of urea, KI, KCl, K_2SO_4, and sucrose. After drying, these cell-wall-adhesive/Mylar bilayers displayed distinct actuation in response to alternating RH changes between 5% and 90% (**Fig. 1c-h**). Compared to the untreated samples, the

bilayer films treated with 1 mM and 10 mM sucrose and K_2SO_4 solutions exhibited enhanced curvature. However, the curvature decreased when the concentrations of the solutions increased to 30 mM and 50 mM. The bilayer films treated with urea and KI solutions did not show enhanced water-responsiveness; instead, the curvature decreased as the concentration of urea and KI solutions increased from 1 mM to 50 mM (**Fig. 1i**). Based on the curvature at 5% RH, we estimated the WR energy density of the cell-wall-adhesive composites coated on Mylar films (**Fig. 1j**)[42]. We observed that, compared to untreated cell-wall-adhesive composites (3.8 MJ m^{-3}), samples treated with low-concentration (10 mM) kosmotropes of sucrose and K_2SO_4 exhibited increased WR energy densities of 4.5 MJ m^{-3} (an 18.7% increase) and 4.0 MJ m^{-3} (a 6.2% increase), respectively. However, WR energy densities decreased by 52.2% (1.8 MJ m^{-3}) and 41.9% (2.2 MJ m^{-3}) when the concentrations of sucrose and K_2SO_4 solutions were further increased to 50 mM. The samples treated with a moderate kosmotrope, KCl, displayed a trend similar to those treated with sucrose and K_2SO_4, but did not show any significant increase in energy density. In contrast, the cell-wall-adhesive composites treated with chaotropic urea and KI exhibited a monotonic decrease in WR energy densities to 1.6 MJ m^{-3} (a 58.5% decrease) and 2.0 MJ m^{-3} (a 48.3% decrease), respectively, as the solute concentrations increased to 50 mM. These results suggest that treatment with kosmotropic solutions at certain concentrations can enhance the water-responsiveness of cell-wall-adhesive composites.

WR strain and speed of untreated and solute-treated cell walls

To further investigate the effects of nanoconfined liquids' properties on WR actuation of individual cell walls, we used an environment-controlled atomic force microscope (AFM) to measure the WR strain of the cell walls in response to local RH changes (**Fig. 2**). To characterize the WR strain, we

compared the AFM topography of the cell walls at 90% RH to those at 5% RH (**Fig. 2a** and **Fig. S2-6**). We observed that the WR strain of cell walls treated with kosmotropic sucrose, K_2SO_4, and KCl slightly increased from 27.9% (untreated) to 36.6%, 29.3%, and 35.0%, respectively, as the solute concentrations increased to 10 mM. It then decreased to 22.0%, 20.4%, and 26.5% as the solute concentrations were further increased to 50 mM (**Fig. 2c**). However, the WR strain of chaotrope-treated cell walls showed dramatic increases, reaching up to 52.8% (urea, 30 mM) and 38.6% (KI, 30 mM) as the solute concentration exceeded 30 mM (**Fig. 2c**), which differs from the decreased energy densities with increased chaotrope concentrations observed in the bilayers (**Fig. 1j**). The enhanced swelling of the urea- and KI-treated samples is likely due to the chaotropic effects, which disperse and swell cell wall structures as the solute reaches the critical concentration[43,44].

Given the distinct WR behaviors of these cell walls resulting from slight changes in the properties of their confined liquids, we hypothesized that untreated and solute-treated cell walls could belong to the newly discovered class of hydration solids[17]. Accordingly, their WR strain can be predicted by the hygroelastic theory, captured by the following mathematical relationship:

$$\frac{\Delta h}{h} \approx \frac{\lambda}{l} ln(ln(\varrho_0)/ln(\varrho)) \tag{1}$$

where $\frac{\Delta h}{h}$ is the WR strain of the cell walls, λ is the characteristic decay length of hydration force, l is the pore-to-pore distance at 50% RH (which approximately corresponds to the characteristic size of the biomolecules forming the cell wall), ϱ_0 and ϱ are the RH values of the initial state and the final state of the cell walls, respectively[17]. We used equation (1) to fit our measured WR strain data and found that the WR strain of most untreated and solute-treated cell walls aligns well with

7

this hygroelastic model, where the hydration force dominates the WR size change, except for the samples treated with higher concentrations of urea and KI solutions at high RH (**Fig. 2d-h**). These deviations for chaotropes are likely due to increased van der Waals forces among the molecular structures of the cell walls as solute concentrations rise[45]. The characteristic decay length to pore-to-pore distance ratio (λ/l), indicating the changes in hydration force within the untreated and treated cell walls, was also obtained from the fitting (**Fig. 2i**). We found that the λ/l ratios of kosmotrope-treated cell walls follow a similar trend that they first increase as the solute concentration increase to 10 mM, and then decrease as the concentration continues to rise to 50 mM. In contrast, the λ/l ratios of chaotrope-treated cell walls gradually increase as the concentration increases (**Fig. 2i**). Considering the observed WR strain (**Fig. 2c**), it appears that, while chaotropes can enhance the WR deformation, they dramatically reduce the intermolecular interactions in cell walls, and thus reduce the WR energy density. The ability of low-concentration kosmotropes to increase WR energy density could be attributed to their capacity to enhance the intermolecular interactions.

These salts and osmolytes slightly affect the WR speed of the cell walls (**Fig. 3** and **Fig. S7-11**). When the local RH was rapidly alternated between 5 % and 90 %, the untreated cell wall took 0.16 s to absorb water and expand during hydration, and 0.21 s to desorb water and shrink during dehydration (**Fig. 3b**). After treatments, the WR speed remains largely unchanged (**Fig. 3c-e**). However, the dehydration time constants showed a noticeable increase as the solute concentration increased to 50 mM: 0.20 s for urea, 0.27 s for KI, 0.24 s for KCl, 0.39 s for K_2SO_4, and 0.33 s for sucrose (**Fig. 3d**). The observed increase in the dehydration time constant in the solute-treated cell walls could be attributed to the reduced evaporation rate of these salt and osmolyte solutions[46].

8

Nanoconfined-liquid-dependent WR energy density and actuation pressure of untreated and solute-treated cell walls

To quantify the influence of urea, KI, KCl, K_2SO_4, and sucrose solutions on the WR energy output and actuation pressure of individual cell walls, we employed the method that we had previously developed for examining the WR energy density of materials at the nanoscale (**Fig. 4**)[8]. In this method, we used a customized AFM to create a thermodynamic cycle that is composed of four stages (**Fig. 4a**). First, a predetermined external force is applied to the cell wall using AFM, and the local RH is maintained at 5% (**Fig. 4a (1)**). Then, the local RH is increased to 90%, causing the expansion of the cell wall while keeping the force constant (**Fig. 4a (2)**). Subsequently, the force applied by the AFM cantilever is reduced to a minimum level, resulting in further expansion of the cell wall (**Fig. 4a (3)**). In the final stage, the RH decreases back to 5%, and the cell wall shrinks while maintaining the minimum force from the previous stage (**Fig. 4a (4)**). Throughout this thermodynamic cycle, the AFM probe remains in contact with the cell wall, allowing for the detection of the cell wall's deformation. The total work done by the cell wall is determined by the enclosed area of the force-displacement curve (**Fig. 4a**). The WR energy density can be then estimated by dividing the work by the effective volume that contributed to the work given by,

$$E_\rho = \frac{W_{CW}}{V_{eff}} \qquad (2)$$

where E_ρ is the WR energy density of the cell walls, W_{CW} is the WR work done by the cell walls during the thermodynamic cycle, and V_{eff} is the effective volume of the cell walls. The V_{eff} was calculated based on previously reported method that equates the indentation depth and mechanical work between sphere indenter condition and plane indenter condition[8].

9

We found that the measured WR energy densities of individual cell walls aligned well with the trends observed in the bilayer experiment (**Fig. 1j, Fig. 4b-h, and Fig. S12-16**). As the solute concentrations increased from 1 mM to 50 mM, the WR energy densities of kosmotrope-treated cell walls initially increased at 10 mM, and then decreased compared to that of the untreated sample (83.2 MJ m^{-3}) (**Fig. 4h**). Remarkably, the cell walls treated with a 10 mM sucrose solution showed an exceptional WR energy density of 103.3 MJ m^{-3}, surpassing those of all known actuator materials[6,8]. The urea- and KI-treated cell walls exhibited monotonic decrease in energy density to 47.4 MJ m^{-3} and 45.3 MJ m^{-3}, as the concentration of solutions increased to 50 mM (**Fig. 4h**). The WR actuation pressure of the cell walls (equivalent to the pressure applied by the AFM probe), where the cell walls show their maximum energy densities, also changed in a similar manner (**Fig. 4i**). The cell walls treated with a 10 mM sucrose solution exhibited the highest WR actuation pressure, reaching 202.5 MPa, which represents a 23.3% increase compared to the untreated case (164.2 MPa). The K_2SO_4- and KCl-treated cell walls also showed their highest WR pressures of 190.1 MPa and 171.9 MPa, respectively, at 10 mM. As the solute concentration increased further, the WR pressure of all kosmotrope-treated cell walls decreased. In contrast, the actuation pressure of chaotrope-treated cell walls decreased as the concentration of chaotropes increased. These results suggest that the observed changes in the WR energy densities of treated cell walls were dominated by the change in WR pressure rather than the WR strain. For example, although treatments with 30 mM and 50 mM urea and KI dramatically enhanced the cell wall's WR strain (**Fig. 2c**), the WR pressure and energy densities decreased significantly compared to the untreated samples (**Fig. 4h, i**). It is clear that the water-responsiveness of the cell wall is highly sensitive to the properties of nanoconfined liquids. Even slight alterations of these properties through low-

concentration chaotropes and kosmotropes can result in significant changes in WR pressure and energy. Our observations also suggest the existence of an optimal range for kosmotropic and chaotropic treatments to maximize WR energy density. Beyond this range, both WR actuation pressure and energy density decrease. It is noteworthy that while both high-concentration kosmotropes and chaotropes decrease WR pressure and energy density, their mechanisms differ significantly. Kosmotropes tend to aggregate cell wall structures and restrict the WR strain (**Fig. 2c, i**), thereby limiting the transfer of intermolecular forces to macroscopic WR pressure. In contrast, chaotropes swell cell wall structures and reduce intermolecular interactions, leading to decreased WR pressure.

IR spectra of untreated and solute-treated cell walls

The intermolecular interactions of untreated and solute-treated cell walls were further investigated using an environment-controlled Fourier transform infrared spectroscopy (FTIR). The observed amide I (1648 cm^{-1}) and amide II (1546 cm^{-1}) spectra of untreated cell walls agree with those reported in previous studies (**Fig. 5a, b**)[47]. When the RH increased from 10% to 90%, the amide I peak of both untreated and solute-treated cell walls showed a slight shift to lower wavenumbers, whereas the amide II peak shifted to higher wavenumbers (**Fig. 5b**). These shifts of amide peaks are likely caused by the changes in stress during WR actuation, which was also observed in previous studies[14].

To assess how chaotropic or kosmotropic solutes affect water interactions within cell walls, we deconvoluted the hydroxyl (O-H) stretching band (2800-3750 cm^{-1}) with four Gaussian components, following the method reported in previous studies[48,49] (**Fig. 5c, d** and **Fig. S17-19**).

11

In this approach, lower wavenumbers indicate stronger H-bonding interactions with cell walls and solutes (bound water), while higher wavenumbers correspond to weaker or negligible interactions (bulk water)[50,51]. By comparing the relative amounts of bulk water and bound water in untreated and solute-treated cell walls, we found that kosmotropic solutes enhance H-bonding interactions. Specifically, the amount of bound water at 90% RH increased from 39.1% in untreated cell walls to 43.1% and 45.6% in cell walls treated with 50 mM K_2SO_4 and sucrose solutions, respectively (**Fig. 5e**). In contrast, chaotropic solutes weaken H-bonding interactions, with the amount of bound water decreasing to 34.1% and 37.0% in cell walls treated with 50 mM KI and urea solutions, respectively. The effects of other concentrations (1, 10, and 30 mM) on the relative amounts of bulk and bound water followed a similar trend (**Fig. S17-19**). These results further highlight the significance of H-bonding environments in materials' water-responsiveness and the possibility of controlling this through the addition of kosmotropic and chaotropic solutes.

Discussion

We observed that kosmotropes and chaotropes, which alter the H-bonding network and properties of nanoconfined liquids, can lead to significant changes in the WR strain, speed, pressure, and actuation energy density of *B. subtilis* cell walls. In particular, treatment with low-concentration kosmotropes can increase WR pressure, leading to a significant rise in WR actuation energy density. Conversely, higher concentrations of kosmotropes or any chaotropes reduce WR pressure and energy density. These results could be understood in the light of the hygroelastic theory of hydration solids, which argues that the hydration force generated by the confined water is the dominant mechanism of WR actuation. As the AFM measurements of the cell wall show, the hygroelastic theory successfully predicted the WR strain of the cell wall, providing the first

12

evidence of hydration solids in a material system different from the bacterial spores where the initial discovery was reported[17]. It is therefore possible that changes in the H-bonding environment alter the characteristics of the hydration forces and intermolecular interactions, consequently affecting WR pressure. As a result, the WR actuation energy of cell walls, which is mainly determined by the work done by the hydration force during WR actuation, also changes. Thus, the H-bonding network and the hydration force characteristics appear to play a key role in high-energy WR actuation. Our findings also highlight the potential of using chemical substances to adjust the H-bonding network and intermolecular interactions, ultimately enabling control over the actuation and energy conversion behaviors of hygroscopic materials in a scalable and cost-effective manner.

Methods

Preparation of *B. subtilis* cell walls

B. subtilis cell walls were prepared by following previous protocols[8]. The *B. subtilis* cells were grown by adding 0.5 mL of *B. subtilis* spore suspension (BGA, Sigma Aldrich) in a nutrient broth (Difco, BD) supplemented with 47.2 mg of $Ca(NO_3)_2 \cdot 4H_2O$, 0.44 mg of $FeSO_4 \cdot 7H_2O$, 1 mg of $MnCl_2$ and 0.2 g of glucose (Fisher Scientific)[8]. The *B. subtilis* cells were cultured on a hot plate (Isotemp, Fisherbrand) at 37 °C and vigorous aerobic conditions were maintained using a magnetic stir bar (19 mm × 76.2 mm, Corning) at 200 rpm. After 19 hours, the *B. subtilis* cells were collected from the pellet after centrifuging the cell media suspension at 14,000 × g for 8 min. The collected *B. subtilis* cells were frozen at − 4 °C and thawed at 25 °C 7 times to separate cell wall-bound proteins[52], and then boiled in a 10% w/v sodium dodecyl sulfate (SDS) solution for 3 hours. The resulting cell walls were washed for 5 times with DI water and treated with 10 mL of 2 mg mL^{-1} of pronase (Sigma Aldrich)[53] for protein lysis at 50 °C for 2 hours. Finally, the cell walls were

13

washed with DI water for 5 times and freeze-dried using a lyophilizer (HyperVAC, Grozen). The topography of the isolated cell walls was checked using an AFM and Transmission Electron Microscopy (TEM) (**Fig. S20**). All other chemicals were purchased from Fisher Scientific unless otherwise specified.

Preparation of cell-wall-adhesive/Mylar bilayers

To prepare cell-wall-adhesive/Mylar bilayers, 3 mm × 3 mm × 25 μm Mylar films (Mylar TF-160, Premier Lab supply) were first treated by argon (75%) / oxygen (25%) plasma (Fischione M1070, NanoClean) for 25 s. Subsequently, 8 μL of the cell wall-adhesive suspension consisting of 29.7 mg mL^{-1} of cell walls and 3.05 mg mL^{-1} of a glue (Elmer's glue, Elmer's Product) was deposited on the Mylar films and allowed to dry under ambient conditions. Previous studies have reported that the water-responsiveness of the adhesives were negligible[8].

Solute-treatments of cell walls

To treat the cell-wall-adhesive/Mylar bilayers, the bilayer samples were immersed in urea, KI, KCl, K_2SO_4, and sucrose solutions with various concentrations (1 mM, 10 mM, 30 mM, and 50 mM) for 20 s, followed by blow-drying with nitrogen to eliminate excessive of solution. To treat cell wall samples for AFM measurements, 0.5 μL of untreated cell wall solution (0.3 mg mL^{-1}) was first deposited on a silicon substrate and dried under ambient conditions. After drying, the samples were immersed in urea KI, KCl, K_2SO_4, and sucrose solutions of 1 mM, 10 mM, 30 mM, and 50 mM for 20 s and blow-dried with nitrogen. The cell wall samples for FTIR were prepared similarly. First, 4 μL of the cell wall solution (0.4 mg mL^{-1}) was deposited on a 2-mm-thick calcium fluoride (CaF_2) substrate and dried to form a ~ 20-μm-thick cell wall layer. The samples

14

were immersed in urea, KI, KCl, K_2SO_4, and sucrose solutions with different concentrations for 20 s and blow-dried. The solution concentrations were kept not to exceed 50 mM in order to avoid the saturation effect caused by high ion concentration[54].

WR strain characterization

The WR strain of cell walls was tested by an environment-controlled AFM (Multimode 8, Bruker) at 25 °C. The AFM was customized to control the RH by injecting dry and humid air with a certain ratio. The RH inside the AFM chamber was monitored by a commercial RH sensor (HIH-4021-003, Honeywell). Each RH level was maintained for at least 5 minutes before measurements. The topographic images of the cell walls were obtained using an AFM probe (NCHV, Bruker) at tapping mode and analyzed using the Nanoscope Analysis software (Bruker). The WR strain of the cell walls was calculated by diving the height differences of cell walls between 90% RH and 5% RH by that of 5% RH, given by

$$\varepsilon_s = \frac{(h_{90\% \text{ RH}} - h_{5\% \text{ RH}})}{h_{5\% \text{ RH}}} \times 100 \ (\%) \tag{3}$$

where ε_s is the WR strain, and $h_{90\% \text{ RH}}$ and $h_{5\% \text{ RH}}$ are the heights of the cell walls at 90% RH and 5% RH, respectively.

WR time constant characterization

The WR time constants of the cell walls were determined from the instant height change of the cell walls when responding to alternated RH changes between 5% and 90% RH. The RH was alternated by injecting dry air (5% RH) or humid air (90% RH) controlled by a solenoid valve (VK332Y-6GM5, SMC) with a response time of less than 10 ms. The dynamic height changes of

15

the cell walls were measured by using AFM with a probe (LRCH-250, Team Nanotec) placed on the top surface of the cell walls in real-time. Dehydration and hydration time constants of the cell walls were calculated by fitting the obtained height change to exponential growth and decay functions:

$$\Gamma_{hyd}(t) = (\Gamma_{max} - \Gamma_{min})e^{\frac{-t}{\tau_{hyd}}} + \Gamma_{min} \tag{4}$$

$$\Gamma_{dehyd}(t) = -(\Gamma_{max} - \Gamma_{min})e^{-\frac{t}{\tau_{dehyd}}} + \Gamma_{max} \tag{5}$$

where Γ_{hyd} and Γ_{dehyd} are the dynamic height over time (t) during hydration and dehydration, Γ_{max} and Γ_{min} are the maximum and the minimum height, τ_{hyd} and τ_{dehyd} are the relaxation time constants during hydration and dehydration, respectively.

WR energy density characterization

The WR energy density of the macroscale cell-wall-adhesive composite was estimated from the elastic energy stored in the curved bilayer samples at 5% RH. The elastic energy of the curved bilayers was calculated using previously reported method[8], where the elastic energy U is given by

$$U = \frac{E_m I_m L}{R^2} \tag{6}$$

where I_m is the inertial momentum of the Mylar film, E_m is Young's modulus (3.60 GPa[8]) of the Mylar film, and R is the radius of the bilayer's curvature at 5% RH, analyzed from photographs taken with a DSLR camera (Canon) using the Image J software. The WR energy density, ED, of the cell-wall-adhesive composite is then calculated by dividing the elastic energy by the volume of the composite (V) using,

16

$$ED = \frac{U}{V} \tag{7}$$

The WR energy densities of untreated and solute-treated cell wall samples were obtained from a thermodynamic cycle created by an environment-controlled AFM with a large radius probe (LRCH-250, Team Nanotec), which was reported in previous studies[8]. During the experiment, the RH, the force applied on the cell walls, and the indentation depth were controlled and synchronized by a LabVIEW program and a high-speed data acquisition device (PCI-6115, National Instruments). The cycle time was fixed to 20 s while the applied force was varied to find the maximum WR energy densities and their corresponding actuation pressure (**Fig. S12-16**).

Environment-controlled FTIR

The FTIR (Vertex 70, Bruker) was customized to be environment-controlled. A 300-μm-thick acrylic spacer was placed between the prepared samples and the CaF_2 substrate in the flow cell (Harrick Scientific), which allows the injection of air with a certain RH monitored by a commercial RH sensor (HIH-4021-003, Honeywell). The FTIR spectra of the samples were measured over a wavenumber range of 1500-3750 cm^{-1} in 64 scans at a resolution of 6 cm^{-1}. To analyze H-bonding interactions, the O-H stretching spectra from 2800 cm^{-1} to 3750 cm^{-1} was first baseline-corrected and normalized. Subsequently, the O-H stretching peak was deconvoluted into six Gaussian functions with the following constrained wavenumber ranges: 3080-3110 cm^{-1} for IBW, 3220-3250 cm^{-1} for FBW, 3385-3400 cm^{-1} for INBW, 3520-3550 cm^{-1} for LBW, and 2900-2990 cm^{-1} for two Gaussian components representing C-H vibrations, following methodologies from previous studies[48,49] (see **Supplementary Information, Fig. S17-19,** and **Table S1-4**). All peaks demonstrated a high goodness of fitting, with R^2 values greater than 0.997. The contributions of the two C-H peaks were less than 5.5% and 6% of the total relative area, respectively. The relative

17

amounts of bulk and bound water were estimated by summing the area contributions of INBW and LBW to represent bulk water, and the contributions of IBW and FBW to represent bound water[48,55]. Note that the fitting results slightly vary depending on the fitting parameters used. The O-H stretching spectra for solutions at concentrations of 50 mM, 100 mM, and 500 mM were also measured (**Fig. S21**).

TEM

For TEM experiments, we use grids that were purchased from Electron Microscopy Sciences (Cat# CF400-Cu), which has thin film of pure carbon (5-6 nm) deposited on one side of the grid. All grids with carbon side facing up were cleaned for 35 seconds in Fischione Nanoclean 1070 (70% power) with a mixture of Argon (75%) and Oxygen (25%). 4-5 µl of sample solution was pipetted onto the carbon film side of a freshly cleaned grid. The sample solution was incubated on EM grid for 1 mins and excessive solution was removed with filter paper. Then, it was washed by one drop of DI water that was removed by filter paper. TEM grids were air-dried and then transferred to desiccator for storage. EM grids were later transferred into a single tilt specimen holder that was then inserted into the microscope. Imaging was performed in Titan Halo TEM operating at 300 kV and CETA camera (Thermo Fisher Scientific).

18

Author contributions X.C. conceived and initiated the project. S.K. prepared the cell wall and performed the AFM, FTIR and cell-wall-adhesive bilayer energy density measurements. T.W. performed the TEM measurements. S.K., H.W., and D.P. analyzed the AFM and FTIR data. All authors contributed to data analysis and discussed the results. S.K. and X.C. wrote the paper, and X.C. supervised the project.

Competing interests X.C. and H. W. are the inventors on patent "Water-responsive materials and uses therefor." US Patent 10,961,988 B2, issued on March 30, 2021.

Data availability The data supporting the findings of this study are available from the corresponding authors upon reasonable request.

19

References and Notes:

1. Bar-On, B. *et al.* Structural origins of morphing in plant tissues. *Appl. Phys. Lett.* **105**, 33703 (2014).

2. Rassart, M., Simonis, P., Bay, A., Deparis, O. & Vigneron, J. P. Scale coloration change following water absorption in the beetle Hoplia coerulea (Coleoptera). *Phys. Rev. E - Stat. Nonlinear Soft Matter Phys.* **80**, 1–6 (2009).

3. Rafsanjani, A., Brulé, V., Western, T. L. & Pasini, D. Hydro-responsive curling of the resurrection plant Selaginella lepidophylla. *Sci. Rep.* **5**, 8064 (2015).

4. Reyssat, E. & Mahadevan, L. Hygromorphs: From pine cones to biomimetic bilayers. *J. R. Soc. Interface* **6**, 951–957 (2009).

5. Elbaum, R., Gorb, S. & Fratzl, P. Structures in the cell wall that enable hygroscopic movement of wheat awns. *J. Struct. Biol.* **164**, 101–107 (2008).

6. Park, Y. & Chen, X. Water-responsive materials for sustainable energy applications. *J. Mater. Chem. A* **8**, 15227–15244 (2020).

7. Gravelle, S. *et al.* Optimizing water permeability through the hourglass shape of aquaporins. *Proc. Natl. Acad. Sci. U. S. A.* **110**, 16367–16372 (2013).

8. Wang, H. *et al.* High Energy and Power Density Peptidoglycan Muscles through Super-Viscous Nanoconfined Water. *Adv. Sci.* **9**, 1–11 (2022).

9. Luo, D. *et al.* Autonomous self-burying seed carriers for aerial seeding. *Nature* **614**, 463–470 (2023).

10. Weng, M. *et al.* Multiresponsive Bidirectional Bending Actuators Fabricated by a Pencil-on-Paper Method. *Adv. Funct. Mater.* **26**, 7244–7253 (2016).

11. Jia, T. *et al.* Moisture Sensitive Smart Yarns and Textiles from Self-Balanced Silk Fiber Muscles. *Adv. Funct. Mater.* **29**, 1808241 (2019).

12. Xing, Y., Fei, X. & Ma, J. Ultra-Fast Fabrication of Mechanical-Water-Responsive Color-Changing Photonic Crystals Elastomers and 3D Complex Devices. *Small* **20**, 2405426 (2024).

13. Cakmak, O., El Tinay, H. O., Chen, X. & Sahin, O. Spore-Based Water-Resistant Water-Responsive Actuators with High Power Density. *Adv. Mater. Technol.* **4**, 1800596 (2019).

14. Piotrowska, R. *et al.* Mechanistic insights of evaporation-induced actuation in supramolecular crystals. *Nat. Mater.* **20**, 403–409 (2021).

15. Van Zee, N. J. *et al.* Potential enthalpic energy of water in oils exploited to control supramolecular structure. *Nature* **558**, 100–103 (2018).

16. Sheehan, F. K. *et al.* Aromatic Zipper Topology Dictates Water-Responsive Actuation in Phenylalanine-Based Crystals. *Small* **19**, 1–7 (2023).

17. Harrellson, S. G. *et al.* Hydration solids. *Nature* **619**, 500–505 (2023).

18. Israelachvili, J. N. *Intermolecular and Surface Forces: Third Edition. Intermolecular and Surface Forces: Third Edition* (2011).

19. Calero, C. & Franzese, G. Water under extreme confinement in graphene: Oscillatory dynamics, structure, and hydration pressure explained as a function of the confinement width. *J. Mol. Liq.* **317**, 114027 (2020).

20. Ogbebor, J. *et al.* Ultrasonic study of water adsorbed in nanoporous glasses. *Phys. Rev. E* **108**, 024802 (2023).

21. Hofmeister, F. Zur Lehre von der Wirkung der Salze. *Arch. Für Exp. Pathol. Pharmakol.* **24**, 247–260 (1888).

22. Ninham, B. W. & Yaminsky, V. Ion binding and ion specificity: The Hofmeister effect and Onsager and Lifshitz theories. *Langmuir* **13**, 2097–2108 (1997).

23. Parsons, D. F., Boström, M., Kunz, W. & Ninham, B. W. Hofmeister Effects. *Encycl. Water* 1–7 (2019).

24. Herberhold, H., Royer, C. A. & Winter, R. Effects of Chaotropic and Kosmotropic Cosolvents on the Pressure-Induced Unfolding and Denaturation of Proteins: An FT-IR Study on Staphylococcal Nuclease. *Biochemistry* **43**, 3336–3345 (2004).

25. Baynes, B. M. & Trout, B. L. Rational Design of Solution Additives for the Prevention of Protein Aggregation. *Biophys. J.* **87**, 1631–1639 (2004).

26. Zhang, Y. & Cremer, P. S. Chemistry of hofmeister anions and osmolytes. *Annu. Rev. Phys. Chem.* **61**, 63–83 (2010).

27. Kim, J. S., Wu, Z., Morrow, A. R., Yethiraj, A. & Yethiraj, A. Self-diffusion and viscosity in electrolyte solutions. *J. Phys. Chem. B* **116**, 12007–12013 (2012).

28. Lo Nostro, P. & Ninham, B. W. Hofmeister phenomena: An update on ion specificity in biology. *Chem. Rev.* **112**, 2286–2322 (2012).

29. Ball, P. & Hallsworth, J. E. Water structure and chaotropicity: Their uses, abuses and biological implications. *Phys. Chem. Chem. Phys.* **17**, 8297–8305 (2015).

30. Marcus, Y. Effect of ions on the structure of water. *Pure Appl. Chem.* **82**, 1889–1899 (2010).

31. Corridoni, T., Mancinelli, R., Ricci, M. A. & Bruni, F. Viscosity of aqueous solutions and local microscopic structure. *J. Phys. Chem. B* **115**, 14008–14013 (2011).

32. Jones, G. & Dole, M. The viscosity of aqueous solutions of strong electrolytes with special reference to barium chloride. *J. Am. Chem. Soc.* **51**, 2950–2964 (1929).

33. Choi, W. S., Patel, D. & Han, J. H. Effects of pH and Salts on Physical and Mechanical Properties of Pea Starch Films. *J. Food Sci.* **81**, E1716–E1725 (2016).

34. Lin, J., Huang, Y. & Wang, S. The Hofmeister effect on protein hydrogels with stranded and particulate microstructures. *Colloids Surf. B Biointerfaces* **196**, 111332 (2020).

35. Majibur Rahman Khan, M., Gotoh, Y., Morikawa, H. & Miura, M. Surface Morphology and Properties of *Bombyx mori* Silk Fibroin Fiber Treated with I_2-KI Aqueous Solution. *Text. Res. J.* **79**, 1305–1311 (2009).

36. Jaspers, M., Rowan, A. E. & Kouwer, P. H. J. Tuning Hydrogel Mechanics Using the Hofmeister Effect. *Adv. Funct. Mater.* **25**, 6503–6510 (2015).

37. Vasanthan, N. *et al.* Lewis acid-base complexation of polyamide 66 to control hydrogen bonding, extensibility and crystallinity. *Polymer* **45**, 4077–4085 (2004).

38. Bennion, B. J. & Daggett, V. The molecular basis for the chemical denaturation of proteins by urea. *Proc. Natl. Acad. Sci.* **100**, 5142–5147 (2003).

39. Huang, Z., Hua, W., Verreault, D. & Allen, H. C. Salty glycerol versus salty water surface organization: Bromide and iodide surface propensities. *J. Phys. Chem. A* **117**, 6346–6353 (2013).

40. Allison, S. D., Chang, B., Randolph, T. W. & Carpenter, J. F. Hydrogen Bonding between Sugar and Protein Is Responsible for Inhibition of Dehydration-Induced Protein Unfolding. *Arch. Biochem. Biophys.* **365**, 289–298 (1999).

41. Chen, H. *et al.* Strong fish gelatin hydrogels enhanced by carrageenan and potassium sulfate. *Food Hydrocoll.* **119**, (2021).

42. Jung, Y. *et al.* Tuning water-responsiveness with *Bombyx mori* silk-silica nanoparticle composites. *Soft Matter* **17**, 7817–7821 (2021).

43. Aroti, A., Leontidis, E., Dubois, M. & Zemby, T. Effects of monovalent anions of the Hofmeister series on DPPC lipid bilayers part I: Swelling and in-plane equations of state. *Biophys. J.* **93**, 1580–1590 (2007).

44. Zangi, R. Can Salting-In/Salting-Out Ions be Classified as Chaotropes/Kosmotropes? *J. Phys. Chem. B* **114**, 643–650 (2010).

45. Kilpatrick, J. I., Loh, S. H. & Jarvis, S. P. Directly probing the effects of ions on hydration forces at interfaces. *J. Am. Chem. Soc.* **135**, 2628–2634 (2013).

46. Rana, B., Fairhurst, D. J. & Jena, K. C. Investigation of Water Evaporation Process at Air/Water Interface using Hofmeister Ions. *J. Am. Chem. Soc.* **144**, 17832–17840 (2022).

47. Hong, Z. N., Jiang, J., Li, J. Y. & Xu, R. K. Preferential adhesion of surface groups of Bacillus subtilis on gibbsite at different ionic strengths and pHs revealed by ATR-FTIR spectroscopy. *Colloids Surf. B Biointerfaces* **165**, 83–91 (2018).

48. Baum, M., Rieutord, F., Juranyi, F., Rey, C. & Rébiscoul, D. Dynamical and Structural Properties of Water in Silica Nanoconfinement: Impact of Pore Size, Ion Nature, and Electrolyte Concentration. *Langmuir* **35**, 10780–10794 (2019).

49. Mansas, C. *et al.* Drivers of Water Transport in Glass: Chemical or Topological Effect of the Glass Network? *J. Phys. Chem. C* **121**, 16201–16215 (2017).

50. Podbevšek, D. *et al.* The role of water mobility on water-responsive actuation of silk. *Nat. Commun.* **15**, 8287 (2024).

51. Gao, Y. *et al.* A Nanoconfined Water–Ion Coordination Network for Flexible Energy-Dissipation Devices. *Adv. Mater.* **35**, 2303759 (2023).

52. Johnson, B. H. & Hecht, M. H. Recombinant Proteins Can Be Isolated from *E. coli* Cells by Repeated Cycles of Freezing and Thawing. *Nat. Biotechnol.* **12**, 381–384 (1994).

24

53. Atrih, A., Zöllner, P., Allmaierr, G. & Foster, S. J. Structural analysis of Bacillus subtilis 168 endospore peptidoglycan and its role during differentiation. *J. Bacteriol.* **178**, 6173–6183 (1996).

54. Clarke-Sturman, A. J., Pedley, J. B. & Sturla, P. L. Influence of anions on the properties of microbial polysaccharides in solution. *Int. J. Biol. Macromol.* **8**, 355–360 (1986).

55. Onori, G. & Santucci, A. IR investigations of water structure in aerosol OT reverse micellar aggregates. *J. Phys. Chem.* **97**, 5430–5434 (1993).

56. Pasquina-Lemonche, L. *et al.* The architecture of the Gram-positive bacterial cell wall. *Nature* **582**, 294–297 (2020).
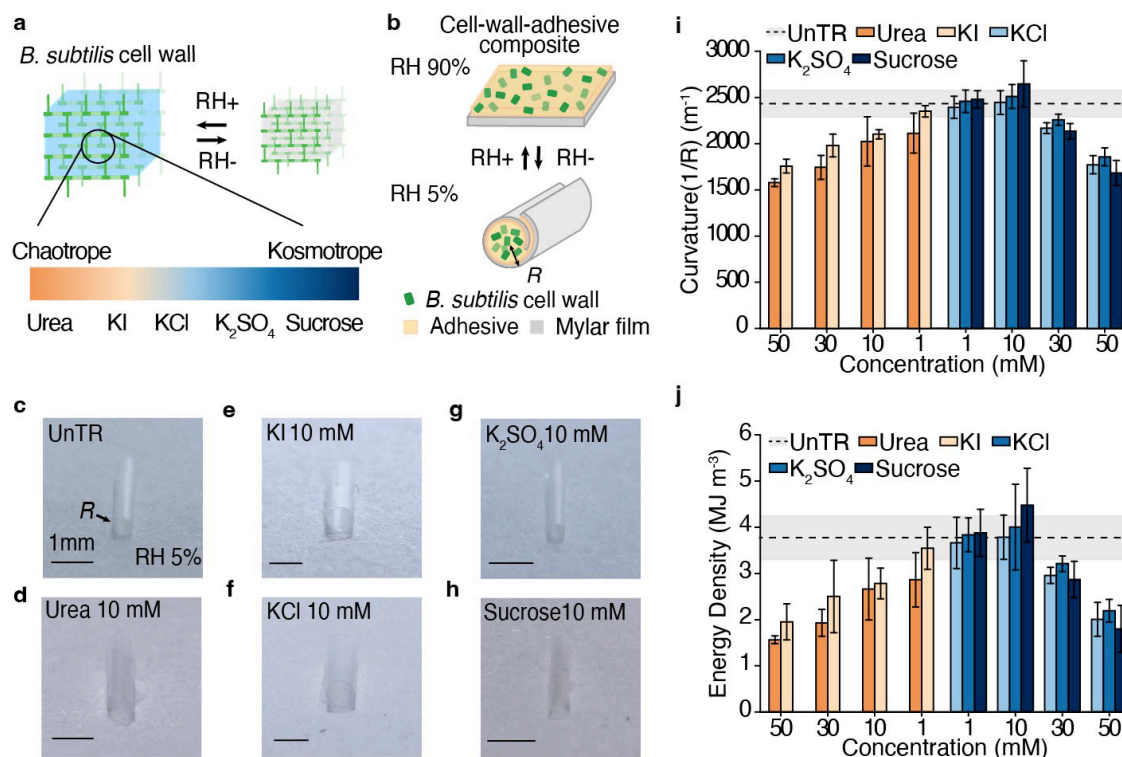
Fig. 1 | The effect of solute treatment on the macroscale water-responsiveness of *B. subtilis* cell walls. a, Alternation of the properties of nanoconfined liquids in porous *B.* subtilis cell walls through treatment with low-concentration chaotrope and kosmotrope solutions. The pore diameters of peptidoglycan, the main component of *B.* subtilis cell walls, vary from approximately 6.8 nm to 38.4 nm[56]. **b**, The cell-wall-adhesive/Mylar bilayers bend and strengthen in response to RH changes between 5% and 90%. **c-h**, Untreated (UnTR) and 10 mM solute-treated cell-wall-adhesive/Mylar bilayers display different curvatures at 5% RH. Scale bar, 1 mm. **i**, Curvature of UnTR and solute-treated cell-wall-adhesive/Mylar bilayers at 5% RH. **j**, WR energy densities of UnTR and solute-treated bilayers estimated from the curvature of the bilayers. The error bars represent the standard errors calculated from five samples.
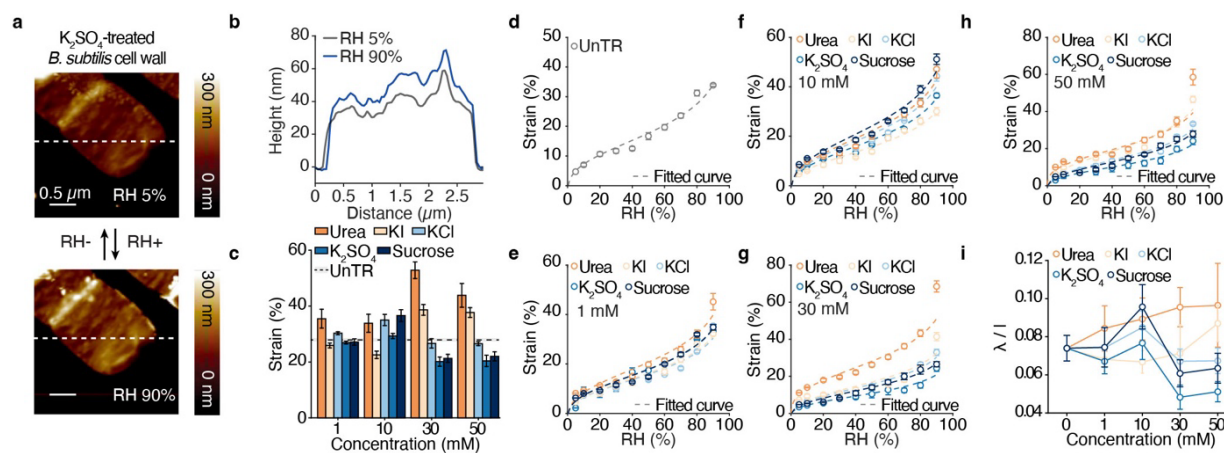
26

Fig. 2 | WR strain of untreated and solute-treated *B. subtilis* cell walls. a-b, AFM topographies (**a**) and cross-section height profiles (**b**) of *B. subtilis* cell walls treated with a 50 mM K_2SO_4 solution at 5% RH and 90% RH. **c**, WR strain of UnTR and solute-treated cell walls. The dashed line represents the WR strain of the UnTR sample, and the grey area indicates the standard error of the UnTR WR strain. The error bars represent the standard errors calculated from five samples. **d-h**, Plots of WR strain *vs.* RH for UnTR cell walls and cell walls treated with solutes at various concentrations: 1 mM (**e**), 10 mM (**f**), 30 mM (**g**), 50 mM (**h**). The dashed line represents the fitted curve of equation (1) to the WR strain (See **Supplementary Note 1**). The error bars in (**d-h**) represent the standard errors of five samples. (**i**) Characteristic decay length to pore-to-pore distance ratio (λ/l) of UnTR and solute-treated cell walls at 50% RH. The error bars in (**i**) represent the 90% confidence band.
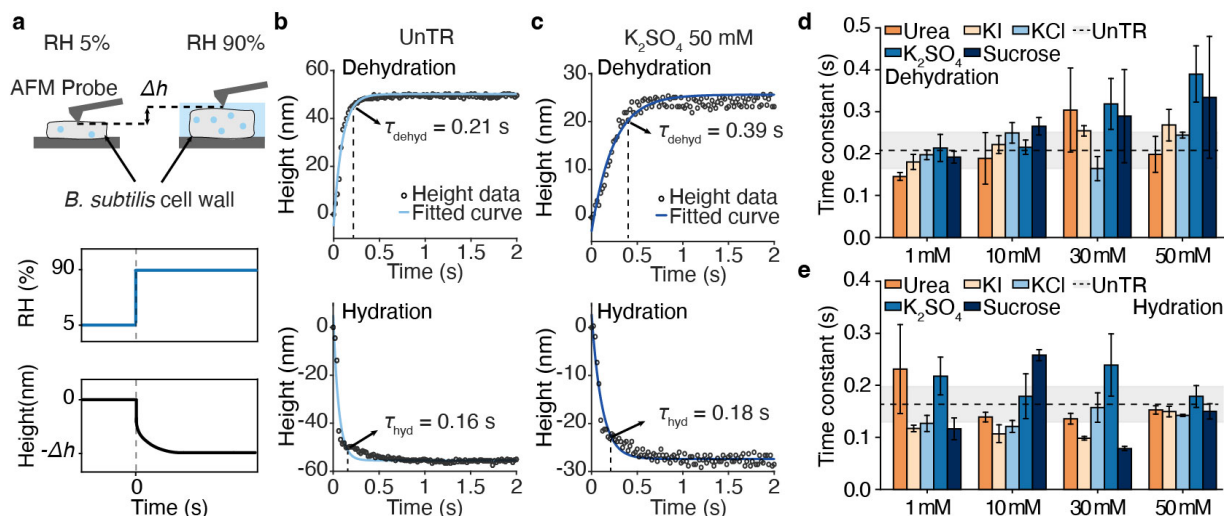
Fig. 3 | WR speed of untreated and solute-treated *B. subtilis* cell walls. a, The AFM was programmed to measure cell wall's height changes in response to rapid RH changes between 5% to 90%. **b-c**, The dynamic height changes of UnTR (**b**) and 50 mM K_2SO_4-treated cell walls (**c**) during dehydration and hydration processes. **d-e**, Dehydration (**d**) and hydration time constants (**e**) of UnTR and solute-treated cell walls. The grey areas represent the standard errors of the UnTR time constants. The error bars represent the standard errors calculated from five samples.
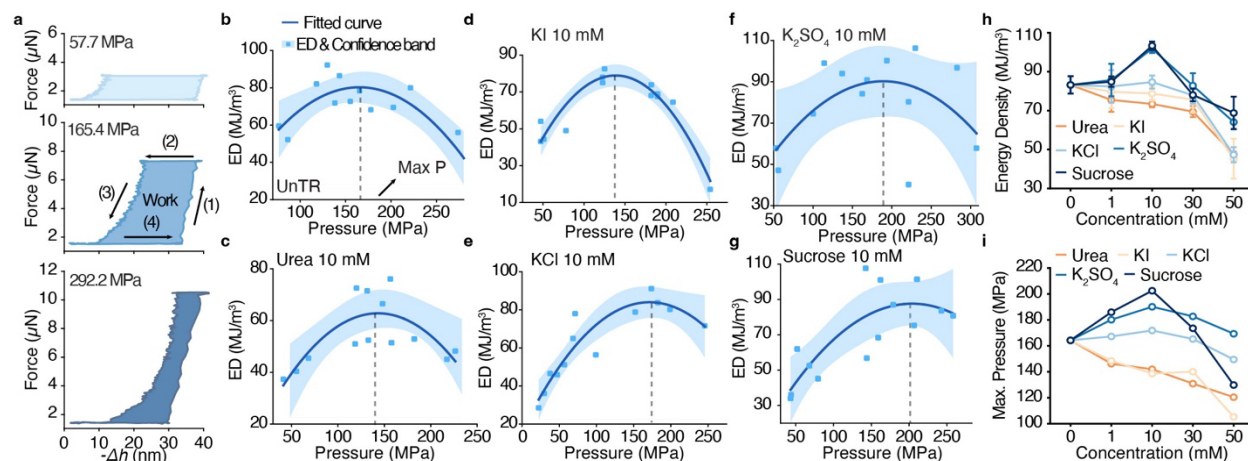
28

Fig. 4 | WR energy density and actuation pressure of untreated and solute-treated cell walls.
a, Force-displacement curves of UnTR cell walls during the thermodynamic cycles with various applied forces. **b-g**, Plots of WR energy density (ED) *vs.* actuation pressure for UnTR (**b**) and 10 mM solute-treated cell walls: urea (**c**), KI (**d**), KCl (**e**), K_2SO_4 (**f**), and sucrose (**g**). The maximum actuation pressure was obtained by fitting the WR energy density *vs.* actuation pressure plots to a quadratic function. The light blue areas represent the 95% confidence band, and the dashed line shows the maximum actuation pressure of the cell walls when they display their maximum energy density. **h**, WR energy density of UnTR and solute-treated cell walls. The error bars represent the standard errors calculated from three maximum EDs **i,** Maximum actuation pressure of the UnTR and solute-treated cell walls at their maximum WR energy density.
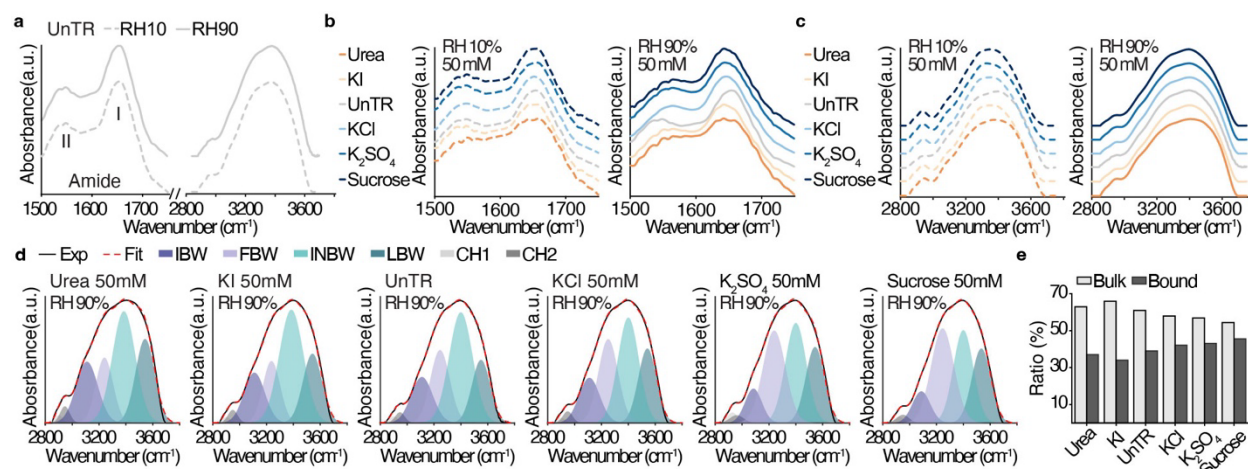
Fig. 5 | FTIR of untreated and solute-treated cell walls. a, IR spectra of untreated cell walls was collected from 1500 cm^{-1} to 1750 cm^{-1} and 2800 cm^{-1} to 3750 cm^{-1} at 10% and 90% RH. **b**, Amide I and II peaks of untreated and 50 mM solute-treated cell walls at 10% and 90% RH. **c**, O-H stretching bands of untreated and 50 mM solute-treated cell walls at 10% and 90% RH. **d**, The deconvolution of O-H stretching bands for 50 mM untreated and solute-treated cell walls at 90% RH. The O-H stretching band was deconvoluted using four Gaussian functions to represent different water populations: 3080-3110 cm^{-1}, ion bonded water (IBW); 3220-3250 cm^{-1}, fully bonded water (FBW); 3385-3400 cm^{-1}, intermediate bonded water (INBW); and 3520-3550 cm^{-1}, low bonded water (LBW), along with two Gaussian functions (2900-2990 cm^{-1}) associated with C-H vibrations. **e**, The relative amounts of bound (IBW+FBW) and bulk (INBW+LBW) water in untreated and 50 mM solute-treated cell walls at 90% RH.